RSC Advances

PAPER

View Article Online
View Journal | View Issue

Cite this: *RSC Adv.*, 2023, **13**, 5957

Direct Z-scheme P–TiO_2/g-C_3N_4 heterojunction for the photocatalytic degradation of sulfa antibiotics†

Dai Yongheng,[a] Yuan Huayu,[a] Li Jiang, *[ab] Su Qi,[a] Yi Qianwen[a] and Zhang Yuntao[a]

The construction of direct Z-scheme heterojunctions with high photocatalytic degradation ability is important for wastewater treatment, but there are still many unsolved challenges. In this article, we report the fabrication of a Z-scheme P–TiO_2/g-C_3N_4 (CNPT-X) heterostructure by the calcination method. Under simulated sunlight, CNPT-X composites are found to show excellent degradation performance against sulfonamide antibiotics sulfadiazine (SD), sulfamethazine (SM2), sulfamonomethoxine (SMM), and sulfamethoxazole (SMZ). CNPT-3 (400 mg L^{-1}) can be used to degrade four sulfa antibiotics within 90 min, with a degradation rate as high as 99%, which is higher than that for P–TiO_2 and g-C_3N_4 alone. The internal electron transfer paths and mechanisms for the composites are revealed by ESR radical detection experiments, XPS energy spectrum shifts, valence band positions and active material quenching experiments. Furthermore, the degradation products are analyzed by GC-MS, and four possible degradation pathways for sulfonamide pollutants are proposed. This photocatalyst provides new insights into the fundamental aspects of the photocatalytic degradation mechanism for composite pollutants, as well as new ideas for practical environmental applications.

Received 16th November 2022
Accepted 17th January 2023

DOI: 10.1039/d2ra07289k

rsc.li/rsc-advances

1 Introduction

Antibiotics are widely present in the environment due to their widespread use in modern medicine,[1,2] therefore, the antimicrobial and antibiotic resistance caused by the misuse or overuse of antibiotics represents a growing and significant threat to global public health.[3] Since the discovery of penicillin in 1929, antibiotics have been widely used to treat bacterial infections in humans and animals for decades,[4] and global antibiotic consumption has increased by 65% from 2000 to 2015.[5] Based on their pharmacological properties, the main categories of antibiotics include aminoglycosides, β-lactams, glycopeptides, macrolides, quinolones, sulfonamides (SAs), and tetracyclines.[6] SAs are broad-spectrum bacteriostatic antibiotics that have been shown to stimulate microbial resistance to sulfonamides even at ppt to ppb levels.[7] The concentration of SAs ranks No. 2 only after tetracyclines in pharmaceutical wastewater, influents, and effluents of wastewater treatment plants (WWTPs), and natural water, with concentrations ranging from μg L^{-1} to mg L^{-1},[8,9] and more than 20 000 tons of SAs are introduced into the biosphere every year.[10] In the Yangtze River Delta Reservoir in East China, SD and SMZ were detected at levels of 92.31% and 100%, with concentrations of 20.82 and 1.26–51.86 ng L^{-1}, respectively,[11] and the maximum concentration of SMM in the Beihe River was found to exceed 300 ng L^{-1}.[12] Therefore, there is an urgent need to develop a cost-effective method to degrade SAs without causing pollution to the environment.

Photocatalysis, as an environmentally friendly technology, not only can be used to degrade a variety of organic pollutants but also has the advantages of safety, nontoxicity, high stability, no secondary pollution, and recyclability of catalytic materials.[13] In 1972, Honda and Fujishima proposed the electrochemical photolysis of water on a TiO_2 semiconductor electrode, paving the way for the utilization of artificial solar energy.[14] Thus, photocatalysis has attracted widespread attention and shows great potential for various solar-driven reactions, such as CO_2 reduction, pollutant degradation, and water splitting.[15–18] However, the main shortcoming of TiO_2 is manifested by its large band gap, which can only utilize ultraviolet radiation,[19] and the application of such photocatalytic materials in practical engineering remains insufficient, especially from the aspects of stability under practical conditions, utilization of solar energy, and the recycling and reuse of catalysts.[20–22] To improve the photoreduction performance, researchers have used various methods to modify TiO_2, such as heterojunctions.[23]

g-C_3N_4 is a polymer inorganic nonmetallic photocatalyst that shows visible light responsiveness, with C and N atoms that are sp^2 hybridized to form a structure with a highly delocalized π-

[a]College of Resources and Environmental Engineering, Guizhou University, Guiyang, 550025, Guizhou, P. R. China. E-mail: jli82@gzu.edu.cn
[b]Guizhou Karst Environmental Ecosystems Observation and Research Station, Ministry of Education, Guiyang, 550025, Guizhou, P. R. China

† Electronic supplementary information (ESI) available. See DOI: https://doi.org/10.1039/d2ra07289k

conjugated system.[24,25] g-C_3N_4 has been widely used for hydrogen conversion,[26] carbon dioxide reduction,[27] and removal of organic pollutants,[28] because it has high thermal and chemical stability. However, the photocatalytic performance of g-C_3N_4 is affected by its small specific surface area, fast electron–hole recombination rate and low visible light utilization rate.[29] In recent years, the photocatalytic performance of g-C_3N_4 has been improved by using various approaches, such as element doping,[30] morphology control and surface modification.[29] The construction of heterojunctions can enable one to enhance the photocatalytic degradation activity of g-C_3N_4,[31] and the oxidation and reduction abilities can be enhanced by using composite materials with a more negative CB and more positive VB.[32] Therefore, it is important to design and prepare photocatalysts with heterojunctions with synergistic effects for adsorption and degradation performance.[33]

In this work, we designed and synthesized P–TiO_2/g-C_3N_4 composites based on thermal condensation reactions for the photocatalytic degradation of mixed sulfonamide antibiotics under simulated sunlight. Through characterization, the energy band structure of the composites is found to conform to the Z-scheme mechanism, and a photocatalytic degradation mechanism is proposed.

2 Materials and methods

2.1 Materials

SD (98%), SM2 (98%), SMM (98%), SMZ (98%), urea, *n*-butyl titanate, *n*-butanol, and ammonium dihydrogen phosphate were all purchased from Aladdin Reagent Co., Ltd (Shanghai, China). Potassium dichromate ($K_2Cr_2O_7$, AR, 99.7%), sodium oxalate ($Na_2C_2O_4$, AR, 99.7%), ethanol (AR, 99.7%) and isopropyl alcohol (IPA, AR, 99.7%) were obtained from Sinopharm Chemical Reagents Co., Ltd (Shanghai, China). All reagents were not purified further before use, and deionized water was used throughout the experiments.

2.2 Preparation of P–TiO_2

P–TiO_2 was prepared according to a previously described method.[34] *n*-Butyl titanate was used as the precursor of TiO_2, and hydrated titanium hydroxide was prepared by a neutral amine sol–gel method. *n*-Butyl titanate was added drop by drop to a solution containing 300 mL of *n*-butanol (1–2 drops per min) until a milky white sol was formed. The pH of the solution was adjusted to 7, and then the solution was magnetically stirred for 12 h. Afterward, the solution was placed in a rotary evaporator at 80 °C to remove excess solvent, following which titanium hydroxide hydrate was obtained. Titanium dioxide phosphide was prepared by impregnating titanium hydroxide with an aqueous solution of ammonium dihydrogen phosphate. First, 0.085 g of ammonium dihydrogen phosphate was dissolved in water, and then 2 g of dried titanium hydroxide hydrate was added, followed by stirring for 4 h. Afterward, the solution was dried at 80 °C for 12 h and finally calcined at 600 °C for 4 h to obtain P–TiO_2. On the basis of no added dihydroammonium phosphate, the unphosphated TiO_2/g-C_3N_4 was obtained.

2.3 Preparation of g-C_3N_4

The g-C_3N_4 was prepared using a nitrogen-protected high-temperature calcination method.[35] First, 10 g of urea was placed into a crucible, and then the sample was placed into a programmed temperature-controlled atmosphere furnace and nitrogen was poured and heated at 550 °C for 2 h at a heating rate of 10 °C min^{-1} to obtain g-C_3N_4.

2.4 Preparation of g-C_3N_4/P–TiO_2

The P–TiO_2/g-C_3N_4 composite photocatalytic material was prepared *via* a thermal condensation reaction. First, 50 mL of P–TiO_2 precursor solution with concentrations of 0.2, 0.6, 1.2, and 2.4 mg L^{-1} was ultrasonically dispersed for 10 min, and then 10 g of urea was added. The solution pH was adjusted to 4–5 with 0.1 mol L^{-1} HCI or NaOH solution, and then the solution was magnetically stirred at 40 °C for 4 h. Afterward, the solution was dried at 80 °C for 12 h. Finally, the obtained white solid was placed in a crucible and heated to 550 °C at a programmed heating rate of 10 °C min^{-1} in a nitrogen atmosphere for 2 h. After cooling to room temperature, the obtained yellow solid was ground to a powder, sealed and placed into dry storage. The P–TiO_2/g-C_3N_4 heterostructures prepared with a varying weight ratio of P–TiO_2 to g-C_3N_4 of 1 : 1, 3 : 1, 6 : 1, and 12 : 1 were marked CNPT-1, CNPT-3, CNPT-6 and CNPT-12, respectively.

3 Results and discussion

3.1 Characterization

X-ray diffraction (XRD) was used to characterize the composition and crystal shape of P–TiO_2, g-C_3N_4 and P–TiO_2/g-C_3N_4 photocatalytic materials with different composite ratios roasted at 550 °C, and the results are shown in Fig. 1a. TiO_2 shows diffraction peaks at 25.12°, 36.94°, 48.04°, 54.28°, 62.80°, 68.98°, 70.36° and 75.16°, corresponding to the 101, 103, 200, 105, 204, 116, 220 and 215 crystal planes, respectively, of mineral phase TiO_2 (JCPDS No. 21-1272) with the square structure of anatase.[36] These results are also in good agreement with previous reports.[36,37] When forming the heterostructures, the characteristic diffraction peak pattern for the anatase phase of TiO_2 becomes more obvious with increasing P–TiO_2 content, especially the 101 crystal plane, indicating that the crystallinity of TiO_2 is improved. In previous studies, the loading of phosphorus can lead to the formation of a more stable anatase phase for TiO_2.[38,39] For the g-C_3N_4 sample, the characteristic peak is located on the 002 crystal plane (JCPDS No. 87-1526) at 2θ = 26.05°. The other characteristic peaks are not obvious in the spectrum due to the interlayer superposition of g-C_3N_4,[40] but the characteristic peaks due to P–TiO_2 and g-C_3N_4 at 25.12° and 26.05° can be found in CNPT-6 and CNPT-12. Thus, the P–TiO_2/g-C_3N_4 composite photocatalytic material was successfully synthesized. In addition, there is no obvious impurity peak in

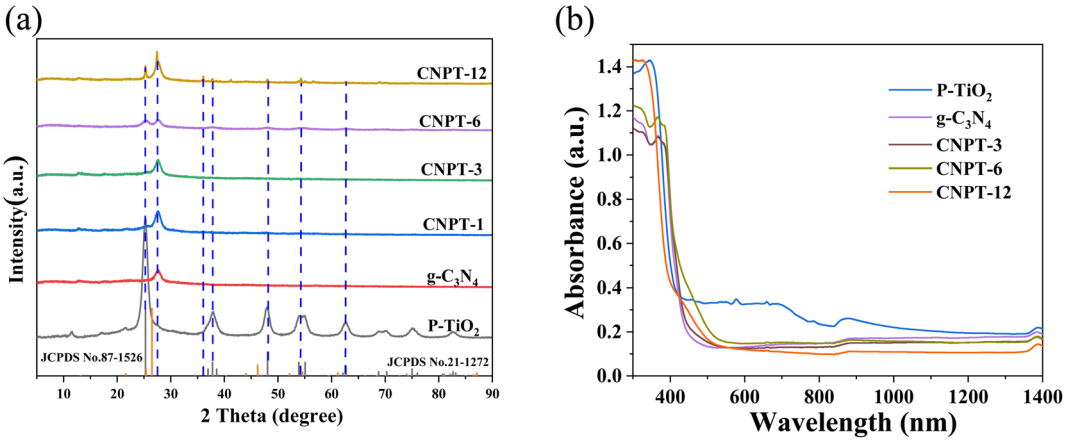

Fig. 1 (a) XRD patterns for g-C_3N_4, P–TiO_2 and P–TiO_2/g-C_3N_4 composite photocatalytic materials; (b) UV-Vis diffuse reflectance spectra for different materials.

the P–TiO_2/g-C_3N_4 composite material, indicating that other impurities are not generated.

UV-Vis DRS was used to analyze the light absorption characteristics of the P–TiO_2/g-C_3N_4 composite photocatalytic material. As shown in Fig. 1b, P–TiO_2 shows strong absorption in the ultraviolet region below 380 nm but weak absorption in the visible region above 400 nm. However, g-C_3N_4 shows obvious absorption above 400 nm, while P–TiO_2 combined with g-C_3N_4 still maintains visible light absorption performance. Compared with P–TiO_2, the light absorption edge of the P–TiO_2/g-C_3N_4 composite photocatalytic material extends to the visible light region.[45] Based on the above analysis, the g-C_3N_4 and TiO_2 composite has a high utilization rate for visible light (>400 nm), which endows the composite photocatalytic material with visible light catalytic activity. At the same time, due to the visible light response capability of g-C_3N_4 and the excellent light scattering performance of the formed heterostructure, the P–TiO_2/g-C_3N_4 composite photocatalytic material exhibits enhanced light absorption performance in both the ultraviolet and visible light regions.

The morphologies of the P–TiO_2, g-C_3N_4 and CNPT-3 catalysts were characterized by scanning electron microscopy (SEM) and transmission electron microscopy (TEM), as shown in Fig. 2. As shown in Fig. 2a, CNPT-3 is composed of clearly wrinkled nanosheets, which have a porous layered morphology and layered structure.[48] In Fig. 2b, the particle size of P–TiO_2 measured by nano measurement software (Nano Measure 1.2) is mainly 7.87–13.74 nm, and the TEM for g-C_3N_4 (Fig. 2c) shows

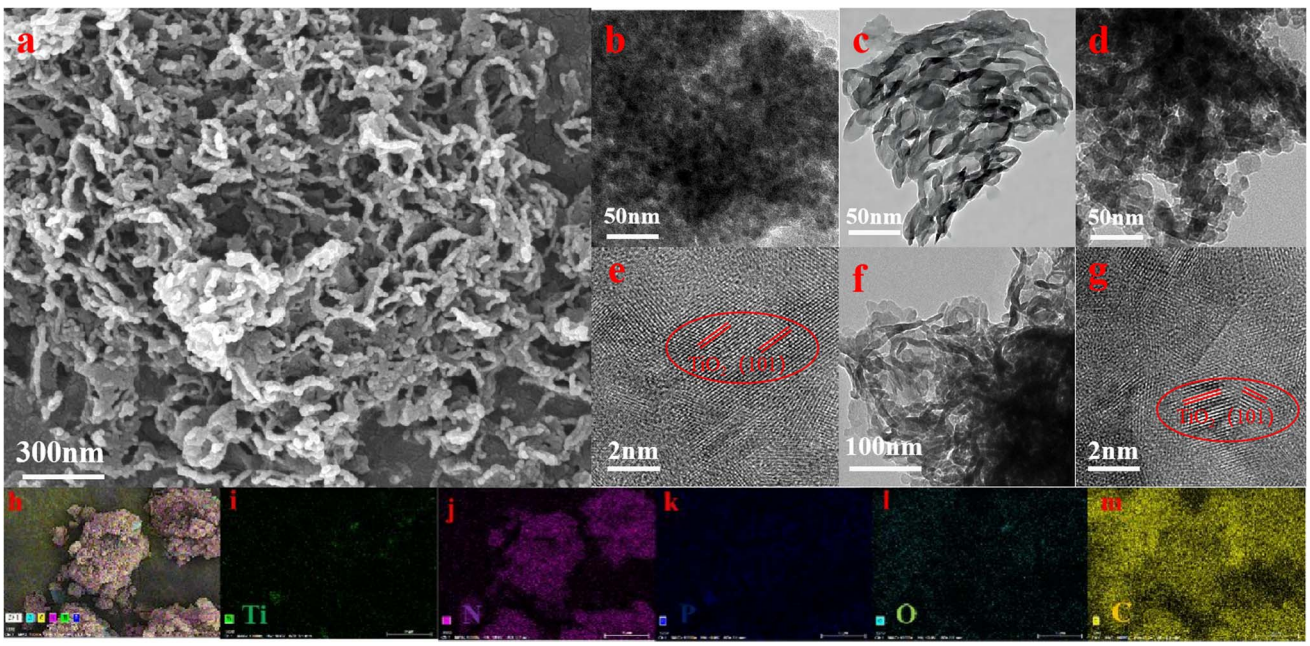

Fig. 2 (a) CNPT-3 composite photocatalytic material SEM; (b) P–TiO_2 and (c) g-C_3N_4 photocatalytic material TEM; (d) and (e) g-C_3N_4/TiO_2 (CNT-3) photocatalytic material TEM; (f) and (g) CNPT-3 photocatalytic material TEM; (h)–(m) CNPT-3 photocatalytic material element mapping.

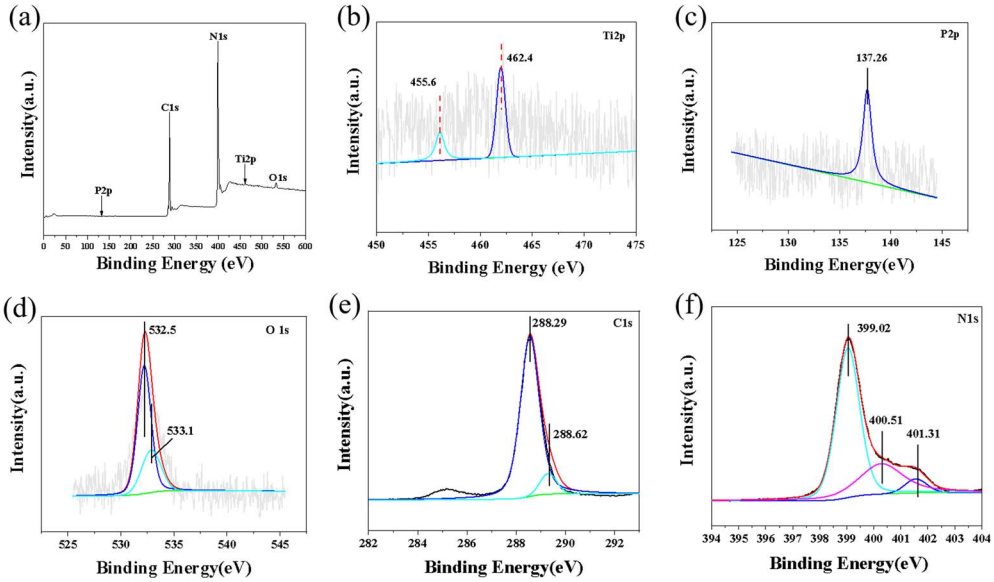

Fig. 3 XPS spectra for P–TiO_2/g-C_3N_4 composite photocatalytic materials: (a) total survey spectrum, (b) Ti 2p, (c) P 2p, (d) O 1s, (e) C 1s, (f) N 1s.

that g-C_3N_4 contains obvious layered pores, and CNPT-3 also shows an obvious pore structure. Therefore, P–TiO_2/g-C_3N_4 composites retain the basic structure of g-C_3N_4.[41] These pore structures can not only provide more photocatalytic active sites but can also show an increased contact area between the antibiotic and the P–TiO_2/g-C_3N_4 composite photocatalyst material, thereby improving the photocatalytic performance of the composite catalyst.[42] Fig. 2d and e display TEM images of the TiO_2/g-C_3N_4 composites that were not phosphated. The picture clearly shows that there are more TiO_2 particle agglomerates on the g-C_3N_4 film. As marked in the picture, the lattice fringes of TiO_2(101) can be clearly observed when the picture is enlarged to 2 nm. Compared with Fig. 2d and f, the particle size of P–TiO_2 loaded onto g-C_3N_4 is smaller than that for TiO_2. As shown in Fig. 2g, it can be observed that the P–TiO_2 and g-C_3N_4 lattice size is 0.302 nm (101) and 0.25 nm (002), respectively, and that the edges are closely connected together, further indicating the formation of a heterojunction between P–TiO_2 and g-C_3N_4. Based on the above analysis, the P–TiO_2/g-C_3N_4 composite material was successfully prepared, and the P–TiO_2 nanoparticles are found to be uniformly deposited onto the g-C_3N_4 nanosheets and show a layered void structure. The elemental mapping images shown in Fig. 2h–m indicate that C, O, Ti, N and P elements are homogeneously distributed within P–TiO_2/g-C_3N_4.[37] These results indirectly demonstrate that the preparation of the P–TiO_2/g-C_3N_4 photocatalytic composite material was successful, which is consistent with the XRD scanning analysis results.

X-ray photoelectron spectroscopy (XPS) was used to research the surface chemical composition and element valence of the P–TiO_2/g-C_3N_4 composite photocatalytic material. As shown in Fig. 3a that P–TiO_2/g-C_3N_4 mainly contains C, O, N, P and Ti, indicating the coexistence of P–TiO_2 and g-C_3N_4 in the nanocomposite. In addition, no characteristic peaks for other elements are observed in the XPS spectrum. As shown in Fig. 3c, the high-resolution P 2p spectrum shows a single peak at 137.26 eV, indicating that phosphorus exists in the P–TiO_2/g-C_3N_4 composite photocatalytic material in the pentavalent oxidation state (P^{5+}).[43] According to previous studies,[38] the electron binding energy of P in P–TiO_2 is increased by 2.66 eV. Fig. 3d shows that the high-resolution O 1s spectrum of P–TiO_2/g-C_3N_4 can be divided into two peaks at 532.5 eV and 533.1 eV, which are attributed to O–Ti bonds and surface –OH groups in the TiO_2 lattice.[44] Phosphorus was found in the P–TiO_2/g-C_3N_4 composite photocatalytic material, indicating that the phosphorus element does not disappear during the preparation of the composite material. The C 1s spectral curve fitting result is shown in Fig. 3e. The characteristic C peak for g-C_3N_4 is located at 288.29 eV, corresponding to the carbon atom of the sp^2 bond of g-C_3N_4. At the same time, the deconvolution of the main peak reveals a subpeak at 287.62 eV. Fig. 3f shows that the high-resolution N 1s spectrum for P–TiO_2/g-C_3N_4 can be divided into three peaks at 401.31, 400.51 and 399.02 eV, which are attributed to amino C–NH_x, tertiary nitrogen N–$(C)_3$ and C=C–N, respectively.[45–47] The XPS results further confirm the successful preparation of the P–TiO_2/g-C_3N_4 composite photocatalytic material.

3.2 Photocatalytic performance for the degradation of antibiotics

Fig. 4a–d show the photocatalytic degradation for different composite ratios of P–TiO_2/g-C_3N_4 on four mixed antibiotics. The data show that P–TiO_2/g-C_3N_4 can achieve a high degradation effect on the four sulfa antibiotics after 120 min of light irradiation. Compared to other photocatalytic materials with different addition amounts, CNPT-3 can achieve high-efficiency degradation for four antibiotics in 30 min: SD: 99.3%, SM2: 99.6%, SMM: 99.6% and SMZ: 99.0%. Compared with g-C_3N_4 alone, the effect of CNPT-3 on the photocatalytic degradation of

sulfonamide antibiotics within 30 min is increased by 1.96 times, 1.94 times, 2.32 times, and 1.02 times for SD, SM2, SMM, and SMZ, respectively, and compared with P–TiO_2 alone, it is increased by 3.06 times, 2.94 times, 2.32 times, and 0.88 times, respectively. However, as the proportion of P–TiO_2 increases, the photocatalytic degradation rate for sulfa antibiotics is decreased. This may be because excessive addition of P–TiO_2 can affect the direct composite effect of g-C_3N_4 and P–TiO_2, and a large amount of P–TiO_2 adheres to the surface of g-C_3N_4 to hinder the contact of active sites with antibiotics. In summary, the P–TiO_2/g-C_3N_4 composite photocatalytic material can be used to achieve a degradation efficiency of more than 97% for mixed sulfonamide antibiotics within 120 min, and CNPT-3 shows a better degradation effect under the condition of 30 min of light irradiation. As shown in the Fig. S1,† the pseudo first-order rate constants (k) of four sulfonamide pollutants are calculated. It is worth noting that CNPT-3 shows the fastest photocatalytic reaction rate, in which SM2, SMM, SD and SMZ are 0.093, 0.112, 0.104 and 0.031 min^{-1} respectively, 2.88, 3.39, 3.05 and 2.82 times of pure g-C_3N_4, and 42.27, 45.90, 52.59 and 6.97 times of pure P–TiO_2. The photocatalytic degradation efficiency of four sulfonamides is SMM > SD > SM2 > SMZ.

To evaluate the influence of different factors on the photodegradation efficiency of sulfonamides, the influence of the initial concentration of sulfonamides is shown in Fig. S2.† When the antibiotic concentration is 3 mg L^{-1}, the photocatalytic degradation effects are SD = 10.2%; SM2 = 10.22%; SMM = 19.95%; SMZ = 17.76%, indicating that the reactive group of the surface of the P–TiO_2/g-C_3N_4 composite photocatalytic material has a low probability of reacting with antibiotics. As the antibiotic concentration is increased from 5 to 10 mg L^{-1}, SD, SM2 and SMM reach a stable degradation effect of more than 92% after 90 min of light irradiation. However, for an antibiotic concentration of 15 mg L^{-1}, the four sulfonamide antibiotics all show poor degradation effects (SD = 90.2%; SM2 = 88.22%; SMM = 80.15%; SMZ = 40.46%). This phenomenon is attributed to the concentration of antibiotics reaching the saturation value of the photocatalytic reaction system, following which the degradation rate decreases with increasing concentration.

The influence of the amount of CNPT-3 catalyst on the degradation efficiency of antibiotics is shown in Fig. S3.† When the P–TiO_2/g-C_3N_4 composite photocatalytic material concentration is 100 mg L^{-1}, the number of active sites is relatively small, and the degradation rate for the four sulfonamide antibiotics after 120 min is small (SD = 13.43%; SM2 = 12.22%; SMM = 10.95%; SMZ = 13.76%). As the concentration of catalytic material is increased from 100 to 700 mg L^{-1}, the degradation rate for the four sulfonamide antibiotics reaches a value of more than 99% because of an increase in the number of catalytic active sites, which can lead to the absorption of more photons to produce active substances. However, for a higher catalyst concentration (1000 mg L^{-1} and 2000 mg L^{-1}), the degradation rate for sulfonamides is reduced. This is due to the

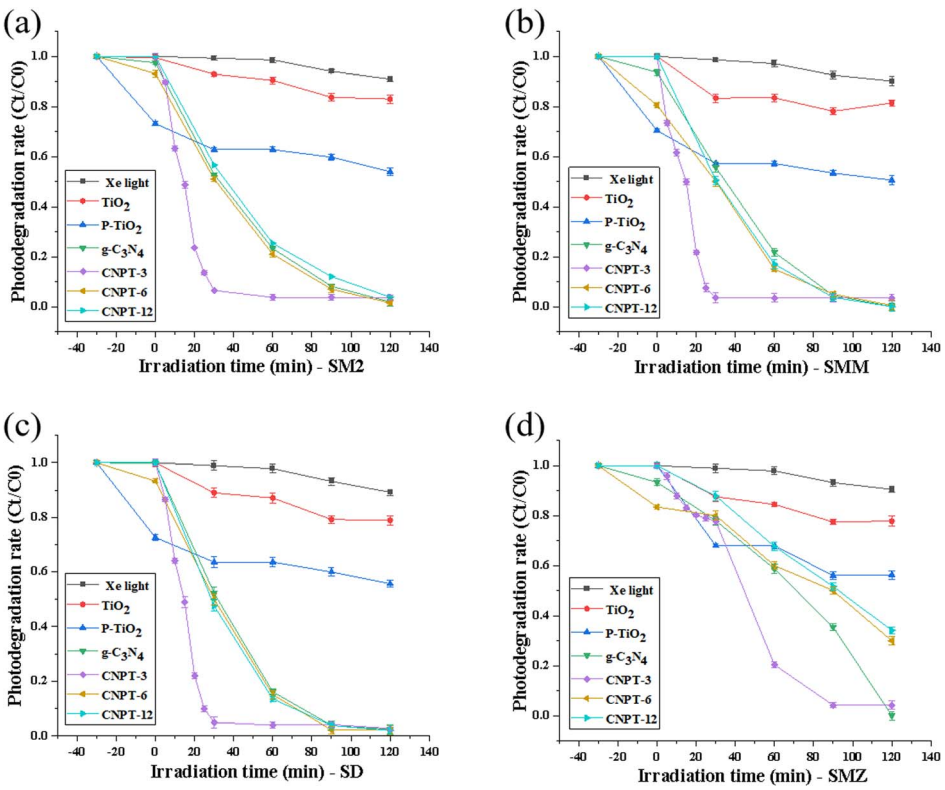

Fig. 4 Degradation effect for four kinds of sulfonamide antibiotics in P–TiO_2/g-C_3N_4 composite photocatalytic materials: (a) SM2, (b) SMM, (c) SD, and (d) SMZ.

agglomeration phenomenon caused by the high catalyst concentration in the stirring process or the high concentration of the catalytic material affecting the permeability of the light beam in the solution preventing the active sites on the surface of the catalyst from absorbing the light intensity.

In addition, the effect of pH on the degradation of sulfonamides by P–TiO_2/g-C_3N_4 is shown in Fig. S4.† The degradation efficiency for sulfonamide antibiotics at pH = 3 and pH = 13 is better than that at pH = 7, indicating that acidic or alkaline conditions are conducive to the degradation of the four mixed sulfonamide antibiotics. Under the condition of pH = 7, the four sulfonamide antibiotics achieve higher degradation effects (SD = 97.61%; SM2 = 98.31%; SMM = 100%; SMZ = 100%). Although the degradation rate of sulfonamide antibiotics can reach a high degradation rate in a short time under the conditions of pH = 3 and pH = 13, considering the actual situation, it is necessary to consider the treatment cost, and secondary treatment under alkaline or acidic conditions under neutral conditions is efficient and environmentally friendly.

3.3 Reusability and stability of the P–TiO_2/g-C_3N_4 composites

The stability of the photocatalyst is one of the most important parameters in the water treatment process. In this study, the stability of P–TiO_2/g-C_3N_4 was determined by recyclability experiments for the photodegradation of four mixed sulfonamide antibiotics. After the end of each cycle, the photocatalyst was recovered through centrifugation, elution and drying before entering the next photocatalytic cycle. As shown in Fig. 5, after three cycles of experiments, the degradation rates for P–TiO_2/g-C_3N_4 for the four sulfonamide antibiotics are SD: 41.35%, SM2: 34.83%, SMM: 52.35% and SMZ: 5.60%.

3.4 Possible photocatalytic mechanism

To analyze the main active substances in the P–TiO_2/g-C_3N_4 composite material in the process of photocatalytic degradation of mixed sulfonamide antibiotics, isopropanol (IPA), benzoquinone (Ben) and sodium oxalate ($Na_2C_2O_4$) were used for quenching reactions to explore the active substances that are beneficial to photocatalytic degradation, and the results are displayed in Fig. S5.[49,50]† Compared with the experimental group without a quencher, the degradation rate for antibiotics after adding benzoquinone, sodium oxalate and isopropanol is decreased to 27.75%, 25.36% and 18.52%, respectively, indicating that $^{\bullet}O_2^-$, h^+ and $^{\bullet}OH$ play a major role in the photocatalytic degradation of mixed sulfonamide antibiotics.

To further confirm the above conclusion, 5,5-dimethyl-1-pyrroline-*N*-oxide (DMPO) was used as a spin trap for ESR analysis. As shown in Fig. S6a,† the $^{\bullet}O_2^-$ signal was not detected in the absence of light irradiation. After the irradiation of the prepared sample with a Xe lamp, a 1 : 1 : 1 : 1 signal peak is observed. As the illumination time is increased, the signal intensity gradually stabilizes. As shown in Fig. S6b,† $^{\bullet}OH$ is also observed in a similar phenomenon, and a 1 : 2 : 2 : 1 signal peak can be observed. Free radical capture experiments and ESR test results show that $^{\bullet}O_2^-$ and $^{\bullet}OH$ radicals are the main active components involved in the photocatalytic degradation process.[41,48,51] It is worth noting that if the charge transfer of the

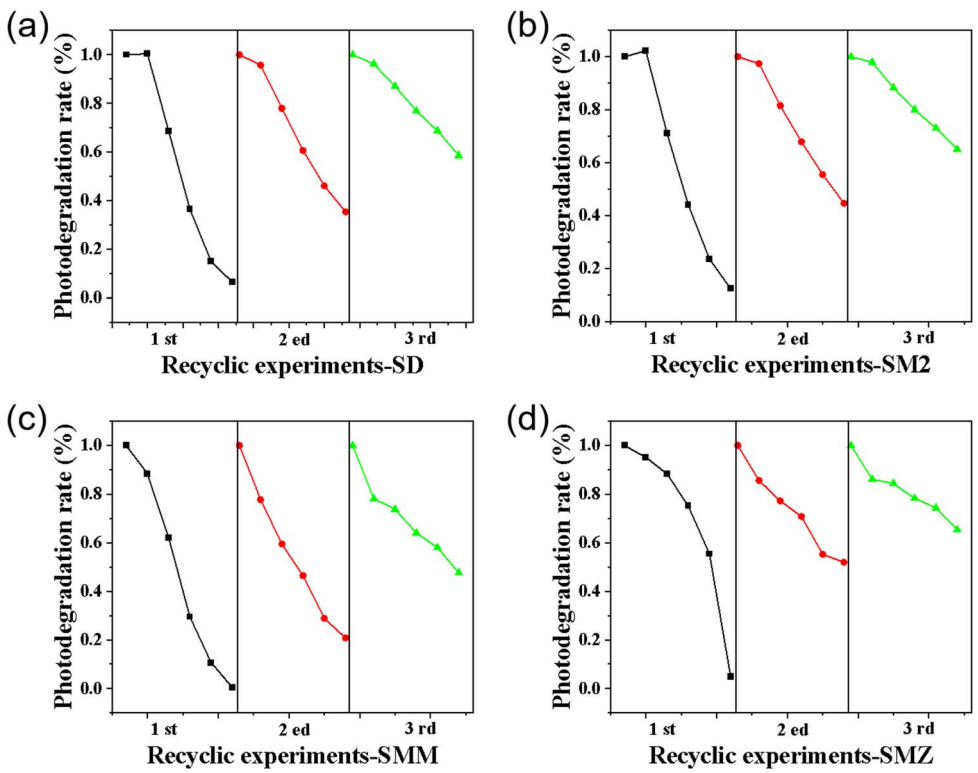

Fig. 5 Stability analysis for the cyclic test for the photocatalytic degradation of antibiotics: (a) SD, (b) SM2, (c) SMM, and (d) SMZ.

complex follows the traditional type II heterojunction mechanism, $^{\cdot}O_2^-$ radicals cannot be generated. Obviously, the Z-scheme heterojunction mechanism is a better candidate for explaining the photocatalyst enhancement mechanism.

The VBXPS energy spectrum was used to measure the valence band positions of g-C_3N_4, P–TiO_2 and P–TiO_2/g-C_3N_4 composite materials, and the band gap energies (E_g) were evaluated using Kubelka–Munk plots:[52]

$$\alpha h\nu = A(h\nu - E_g)n^{1/2}$$

where α, h, ν, and A are the absorption coefficient, Planck constant, light frequency and proportionality constant, respectively.[53] The value for n was selected to be 1/2 for both g-C_3N_4 and P–TiO_2 with a direct bandgap, and E_g was determined from a plot of $(\alpha h\nu)^2$ *versus* $h\nu$.[54] As shown in Fig. 6a, the band gaps (E_g) for g-C_3N_4, P–TiO_2, CNPT-3, CNPT-6 and CNPT-12 were calculated according to the Kubelka–Munk equation to be 2.72 eV, 3.10 eV, 2.79 eV, 2.88 eV and 3.05 eV, respectively. The results show that g-C_3N_4 reduces the band gap of P–TiO_2, but the band gap widths increase with increasing TiO_2 content and further enable the effective formation of heterojunctions between P–TiO_2/g-C_3N_4 composite photocatalytic materials. As shown in Fig. 6b, the valence band edges (VB) of g-C_3N_4, P–TiO_2 and P–TiO_2/g-C_3N_4 are estimated to be 1.60 eV, 2.81 eV, and 2.47 eV according to the XPS valence band spectrum, respectively, and the conduction band edges (CB) for g-C_3N_4 and P–TiO_2 are −0.29 eV and −1.21 eV, respectively.[47] The valence band potential of the P–TiO_2/g-C_3N_4 composite ranges between that of g-C_3N_4 and P–TiO_2 and is close to that of P–TiO_2. This valence band structure conforms to the Z-scheme system configuration, so it can be proven that the band structure of P–TiO_2/g-C_3N_4 has a Z-scheme architecture.[55] In summary, the P–TiO_2/g-C_3N_4 composite photocatalytic material has a Z-scheme energy band structure, and the heterojunction formed between g-C_3N_4 and P–TiO_2 can provide a directional transfer channel for charges, enhance visible light absorption, and reduce the recombination rate for current particles, which further promotes the photocatalytic degradation of antibiotics.[56]

To directly observe the electron transfer direction inside the P–TiO_2/g-C_3N_4 composite material, *in situ* illumination XPS spectroscopy was used for characterization, and the experimental results are shown in Fig. 6c and d. Comparing the Ti 2p energy spectrum and O 1s energy spectrum for TiO_2, P–TiO_2 and P–TiO_2/g-C_3N_4, the P–TiO_2/g-C_3N_4 peak shifts to a high binding energy, and the two elements are mainly derived from P–TiO_2. The peak in the XPS spectrum due to the accumulated electron material shifts to a low binding energy. The peaks in the XPS spectrum shift to a high binding energy for materials that have lost electrons. According to the aforementioned results, the electrons and holes are concentrated in P–TiO_2 and g-C_3N_4 inside the P–TiO_2/g-C_3N_4 composite material, respectively. Such an electron transfer path conforms to the electron transport mechanism of the Z-scheme system, and the XPS spectrum proves that the P–TiO_2/g-C_3N_4 composite material conforms to the Z-scheme system configuration.[57]

The transfer and separation properties for photogenerated carriers of the composite and individual components were investigated by transient photocurrent measurements and electrochemical impedance spectroscopy (EIS).[58] Fig. 6e shows the photocurrent response obtained for P–TiO_2, g-C_3N_4, and P–TiO_2/g-C_3N_4 (CNPT-3) under multiple switching cycles. The results show that CNPT-3 shows the highest photocurrent response intensity, which indicates that CNPT-3 has a better current separation efficiency and longer electron lifetime, much higher than that for a single component.[59] Moreover, this conclusion is also confirmed by the EIS results, as shown in

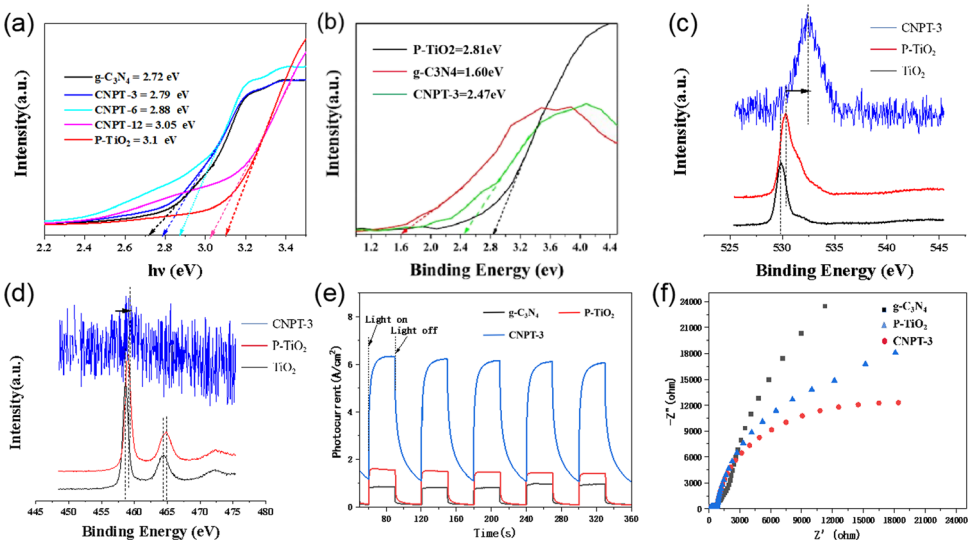

Fig. 6 (a) g-C_3N_4, P–TiO_2 and different ratios of composite band gap width; (b) XPS valence band spectra for the g-C_3N_4, P–TiO_2 and P–TiO_2/g-C_3N_4 composite photocatalytic material (CNPT-3); XPS spectrum migration for the CNPT-3 composites: (c) O 1s, (d) Ti 2p; (e) transient photocurrent response; (f) electrochemical impedance spectroscopy (EIS).

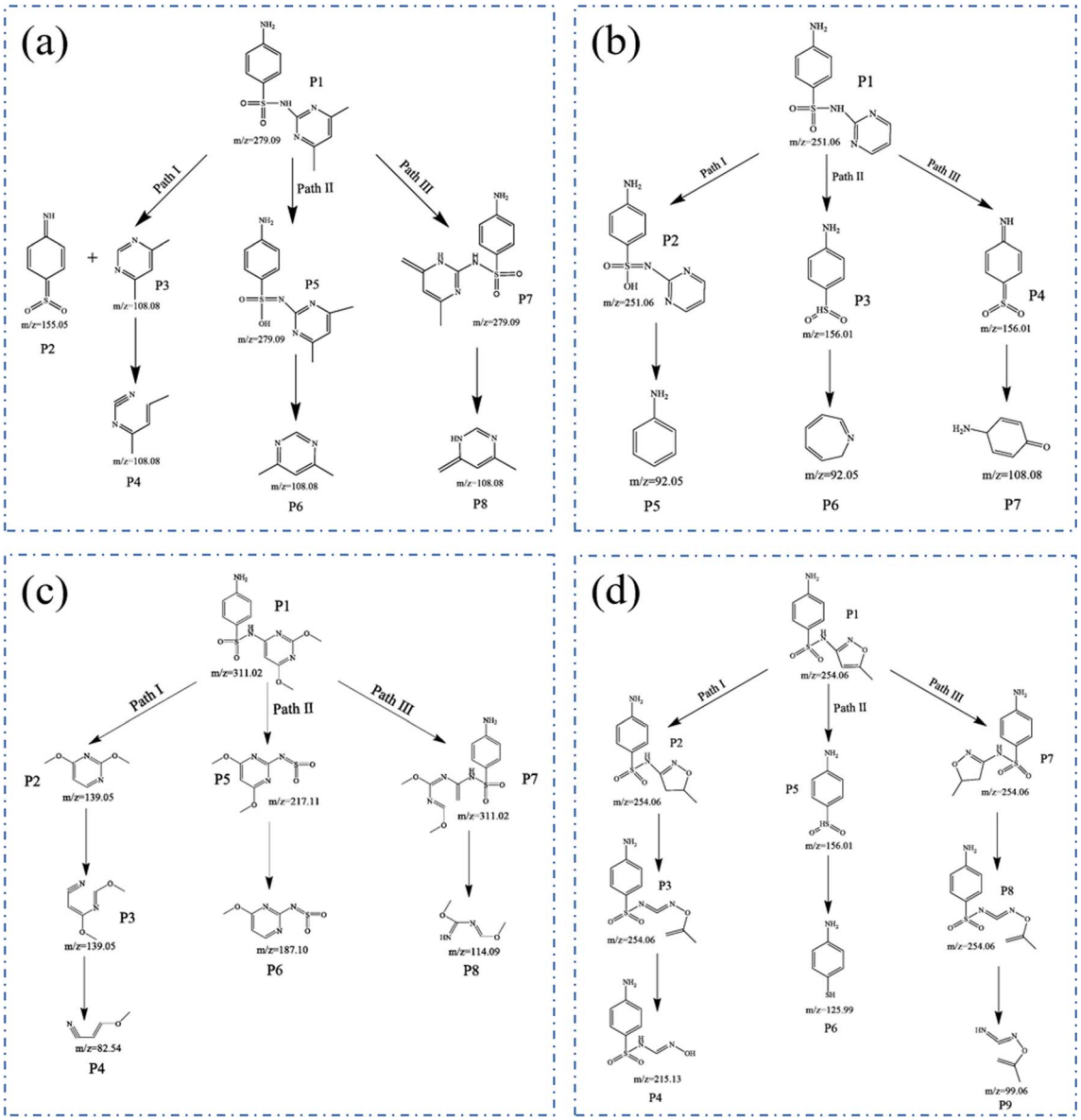

Fig. 7 Possible degradation pathway for (a) SM2; (b) SD; (c) SMM; (d) SMZ.

Fig. 6f. The CNPT-3 shows the smallest arc radius, which indicates the lowest resistance performance, which further indicates that the combination of P–TiO_2 with g-C_3N_4 can significantly reduce the photoresistance and facilitate e^-/h^+ separation.[60] According to the above analysis, the P–TiO_2/g-C_3N_4 heterojunction composite catalyst can lead to a significantly improved visible light response, separation and transfer efficiency for photogenerated carriers, and photodegradation activity for sulfonamide antibiotics.[61] Commonly, the separation rate of photogenerated electrons and holes decreases with an increase in PL emission intensity. Thus, PL spectra were investigated to determine the PL properties and separation ability. Fig. 6a compares the PL intensities of g-C_3N_4, P–TiO_2, and the CNPT-3 composite. CNPT-3 exhibited the lowest PL emission intensity (about 490 nm), which indicated that the introduction of P–TiO_2 played a key role in suppressing the recombination of the photogenerated carriers.

3.5 Analysis of the SA degradation pathway

GC-MS was applied to detect the photocatalytic degradation products of SAs, and the results are displayed in the ESI.†

3.5.1 Degradation pathway for sulfamethazine (SM2). Fig. 7a shows a possible pathway for the photocatalytic degradation of SM2. In path I, P2 and P3 are obtained due to the cleavage of the C–N bond and S–N bonds and the rearrangement of the molecular mechanism. P3 undergoes a ring-opening reaction, the C–N bond is broken, and C≡N is formed. In path II, the aniline is attacked by ·OH, which finally leads to the para-position substitution of the hydroxyl group and the formation of C=N (P5). However, the C–N bond was broken to form P6 in P5. In path III, the molecular structure of

pyrimidine is rearranged to form P7, and finally, the C–N bond is broken to form P8.[64–66]

3.5.2 Degradation pathway for sulfadiazine (SD). Fig. 7b shows a possible pathway for the photocatalytic degradation of SD. Path I can involve attack of ˙OH on the aniline in the SD, leading to the para-substitution of the hydroxyl group to form P2, and finally, breakage of the C–S bond to form P5. Path II can involve the desulfurization reaction caused by the cleavage of N–S and S–C bonds, with the molecular structure rearranged to form a seven-membered heterocyclic compound (P6), followed by release of the sulfur atom on the sulfonamide group in the form of sulfate. Pathway III can involve the cleavage of the N–S bond and the rearrangement of the molecular structure to form two pairs of π–π conjugated structures (P4), and finally, cleavage of the S–C bond, which leads to the desulfurization reaction (P7).[62,63]

3.5.3 Degradation pathway for sulfamonomethoxine (SMM). Fig. 7c shows a possible pathway for the photocatalytic degradation of SMM. In path I, due to the breaking of the C–N bond to form P2, the C–N bond in P2 breaks and forms C≡N(P3), and the C–N bond in P3 continues to break to form P4. In path II, the C–S bond in SMM is broken to form P5, and the C–O bond in P5 is broken to form P6. In path III, the C–C bond of SMM is broken to form P7, and in P7, the C–N bond is broken to form the smaller molecule P8.[67]

3.5.4 Degradation pathway for sulfamethoxazole (SMZ). Fig. 7d shows a possible pathway for the photocatalytic degradation of SMZ. In path I, the C=C bond in SMZ is broken into C–C bonds (P2), the C–C bond in P2 is broken, a ring-opening reaction (P3) occurs, the C–O bond in P3 is broken, and a hydroxylation reaction occurs (P4). In path II, the S–N bond in SMZ is broken to form a smaller molecule P5, and the S=O bond in P5 is broken to form P6. In path III, P7 and P8 undergo the same reaction as in path I, and the S–N bond in P8 is broken to form P9.[68–70]

3.6 Z-Scheme photocatalytic degradation mechanism analysis

Based on the above results and discussion, a photocatalytic mechanism for P–TiO_2/g-C_3N_4 can be proposed. For P–TiO_2, the photogenerated electron–hole pairs easily recombine, and only a part of the photocatalyst participates in the photocatalytic reaction, and the catalytic activity is relatively low. However, for the P–TiO_2/g-C_3N_4 composite material, the surface is partially covered by P–TiO_2 to form a heterojunction, which greatly

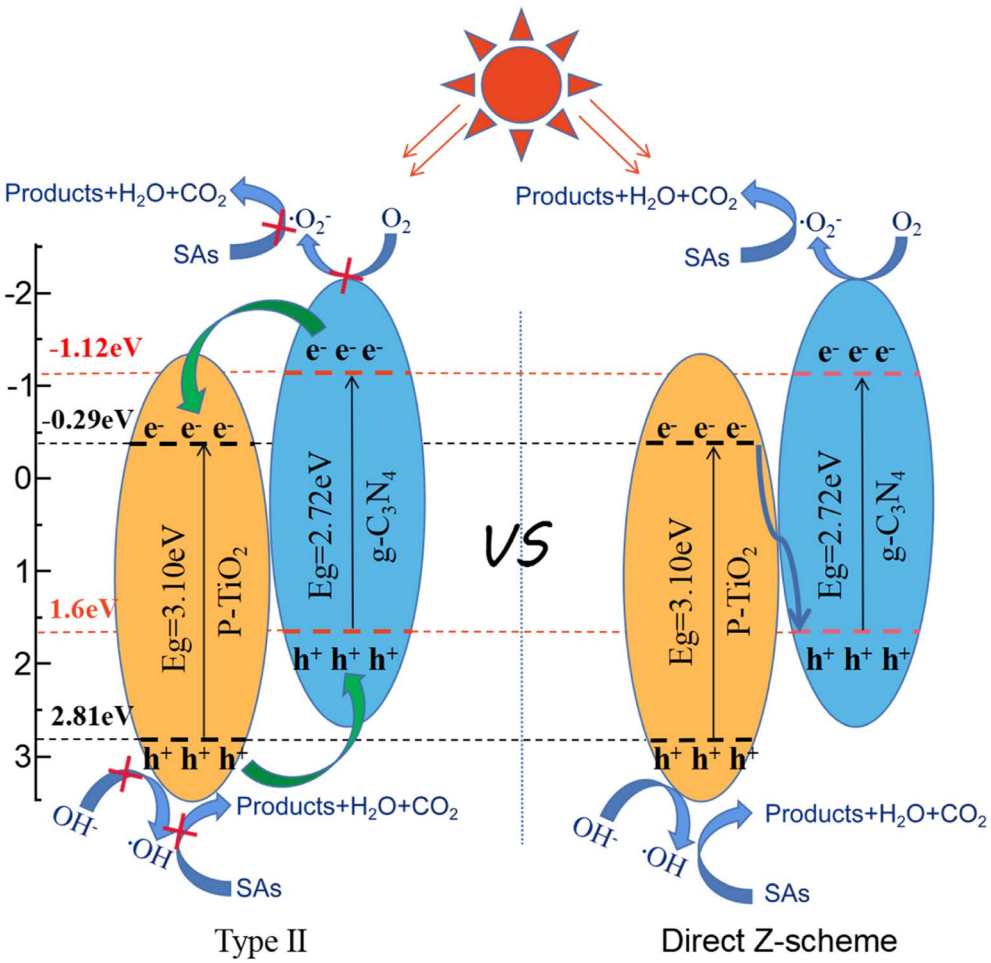

Fig. 8 Schematic diagram of the photocatalytic degradation mechanism.

reduces the recombination efficiency for electron–hole pairs.[51] Fig. 8 presents the Z-scheme photocatalytic degradation mechanism for P–TiO_2/g-C_3N_4. The E_{CB} for P–TiO_2 is −0.29 eV. Because this level is lower than O_2/$^{\bullet}O_2^-$ (−0.33 eV), it cannot participate in the reaction with the dissolved oxygen in the water to form $^{\bullet}O_2^-$. However, O_2/$^{\bullet}O_2^-$ (−0.33 eV) is higher than the E_{CB} (−1.12 eV) of g-C_3N_4, so the photogenerated electrons in the conduction band of g-C_3N_4 can reduce O to $^{\bullet}O_2^-$.[71] The E_{VB} for P–TiO_2 is 2.81 eV, which is higher than that for –OH/$^{\bullet}$OH (2.69 eV), which enables reaction with adsorbed water molecules or hydroxides (–OH) to form hydroxyl groups ($^{\bullet}$OH). Through the quenching experiment for active substances, $^{\bullet}O_2^-$ and $^{\bullet}$OH are known to be the active substances in the system, which play a role in the catalytic process and undergo redox reactions with pollutants to degrade pollutants. The Z-scheme P–TiO_2/g-C_3N_4 composite photocatalytic material can be used to effectively improve the separation of photogenerated electron–hole pairs and greatly reduce the recombination efficiency for electron–hole pairs, thereby improving the photocatalytic activity of the photocatalyst material.[72]

Under light irradiation, the photogenerated electrons generated by the CB of P–TiO_2 can easily migrate to the VB of g-C_3N_4 for the recombination of photogenerated electrons and holes, which then leads to the accumulation of electrons in the CB of g-C_3N_4 and holes in the VB of P–TiO_2. Compared with the direct recombination of electrons and holes in a single material, the effective separation of electrons and holes is achieved after migration through different paths. The photogenerated holes of P–TiO_2 tend to remain in the VB, while electrons are transferred from the CB of P–TiO_2 to the VB of g-C_3N_4. The electron in the VB of g-C_3N_4 is further excited into the CB, which results in the effective separation of photogenerated carriers. Then, the electrons stored on the surface of g-C_3N_4 and the dissolved oxygen present in the water form superoxide radical ions ($^{\bullet}O_2^-$), and the holes generated by P–TiO_2 react with adsorbed water molecules or hydroxide radicals to form hydroxyl groups ($^{\bullet}$OH). Finally, organic pollutants are oxidized to carbon dioxide and water by these highly reactive free radicals. The free radical detection test, XPS energy spectrum shift, valence band position and active substance quenching experiments further confirm the Z-scheme electron transport mechanism. When P–TiO_2 and g-C_3N_4 are combined to form a Z-scheme electron transport, the effective separation for photogenerated carriers can be increased, thereby improving the photocatalytic degradation performance.[73]

4 Conclusions

In this study, Z-scheme heterojunction P–TiO_2/g-C_3N_4 composite photocatalytic materials were prepared to degrade four sulfonamide antibiotics, showing a degradation efficiency of more than 99% after 120 min of illumination, indicating that the P–TiO_2/g-C_3N_4 composite photocatalytic material has an excellent degradation effect on sulfonamide antibiotics. To further understand the possible mechanism for the degradation of sulfonamides, the optical properties and valence band potential of P–TiO_2 were studied by UV-visible diffuse reflectance and valence XPS spectroscopy. The results show that the g-C_3N_4 and TiO_2 composite has a high utilization rate for visible light (>400 nm), which endows the composite photocatalytic material with visible light catalytic activity. The P–TiO_2/g-C_3N_4 composite photocatalytic material has a good energy band structure, and the heterojunction formed between g-C_3N_4 and P–TiO_2 can provide a directional transfer channel for charges, enhance visible light absorption, and reduce the carrier recombination rate, which further promotes the photocatalytic degradation of antibiotics. The quenching experiment proves that $^{\bullet}O_2^-$, $^{\bullet}$OH and h^+ play a major role in the photocatalytic degradation of mixed sulfonamide antibiotics by the P–TiO_2/g-C_3N_4 composite photocatalytic material. Free radical capture experiments and ESR test results show that the $^{\bullet}O_2^-$ and $^{\bullet}$OH radicals produced by the P–TiO_2/g-C_3N_4 composite material under light irradiation are the main active components involved in the photocatalytic degradation process. A free radical detection test, XPS energy spectrum shift, valence band position and active substance quenching experiments further confirm the Z-scheme electron transport mechanism. When P–TiO_2 and g-C_3N_4 are combined to form a Z-scheme, the effective separation of photogenerated carriers is increased due to electron transport, thereby improving the photocatalytic degradation performance. Finally, four sulfonamide degradation products were analyzed by GC-MS, and four possible degradation pathways are proposed, among which the cleavage of S–N, S–C and C–N is concluded to be the main degradation pathway.

Author contributions

Dai Yongheng carried out experiments, formal analyzed data, and drafted the manuscript, Yuan Huayu and Su Qi put forward an original concept at beginning and modified the manuscript. Yi Qianwen and Zhang Yuntao assisted in the experiments. Li Jiang funded the whole study. All authors have read and agreed to the published version of the manuscript.

Conflicts of interest

The authors declare that they have no known competing financial interests or personal relationships that could have appeared to influence the work reported in this paper.

Acknowledgements

This work was supported by Science and Technology Program of Guizhou Provincial of China (No. [2020]1Z051) managed by Jiang Li.

References

1 X. Yang, Z. Chen, W. Zhao, *et al.*, Recent advances in photodegradation of antibiotic residues in water, *Chem. Eng. J.*, 2021, **405**, 126806, DOI: 10.1016/j.cej.2020.126806.
2 Q. Su, J. Li, B. Wang, *et al.*, Direct Z-scheme Bi_2MoO_6/UiO-66-NH_2 heterojunctions for enhanced photocatalytic degradation of ofloxacin and ciprofloxacin under visible

light, *Appl. Catal., B*, 2022, **318**, 121820, DOI: 10.1016/j.apcatb.2022.121820.

3 S. Shao, Y. Hu, J. Cheng, *et al.*, Research progress on distribution, migration, transformation of antibiotics and antibiotic resistance genes (ARGs) in aquatic environment, *Crit. Rev. Biotechnol.*, 2018, **38**(8), 1195–1208, DOI: 10.1080/07388551.2018.1471038.

4 P. R. Burkholder, Antibiotics: the exploitation of microbial antagonisms is having a challenging impact on medicine and society, *Science*, 1959, **129**(3361), 1457–1465, DOI: 10.1126/science.129.3361.1457.

5 E. Y. Klein, T. P. Van Boeckel, E. M. Martinez, *et al.*, Global increase and geographic convergence in antibiotic consumption between 2000 and 2015, *Proc. Natl. Acad. Sci. U. S. A.*, 2018, **115**(15), E3463–E3470, DOI: 10.1073/pnas.1717295115.

6 D. Li and W. Shi, Recent developments in visible-light photocatalytic degradation of antibiotics, *Chin. J. Catal.*, 2016, **37**(6), 792–799, DOI: 10.1016/s1872-2067(15)61054-3.

7 M. Vila-Costa, R. Gioia, J. Aceña, *et al.*, Degradation of sulfonamides as a microbial resistance mechanism, *Water Res.*, 2017, **115**, 309–317, DOI: 10.1016/j.watres.2017.03.007.

8 Y. Deng, B. Li and T. Zhang, Bacteria that make a meal of sulfonamide antibiotics: blind spots and emerging opportunities, *Environ. Sci. Technol.*, 2018, **52**(7), 3854–3868, DOI: 10.1021/acs.est.7b06026.

9 H. Kim, Y. Hong, J. Park, *et al.*, Sulfonamides and tetracyclines in livestock wastewater, *Chemosphere*, 2013, **91**(7), 888–894, DOI: 10.1016/j.chemosphere.2013.02.027.

10 W. Baran, E. Adamek, J. Ziemiańska, *et al.*, Effects of the presence of sulfonamides in the environment and their influence on human health, *J. Hazard. Mater.*, 2011, **196**, 1–15, DOI: 10.1016/j.jhazmat.2011.08.082.

11 C. Cui, Q. Han, L. Jiang, *et al.*, Occurrence, distribution, and seasonal variation of antibiotics in an artificial water source reservoir in the Yangtze River delta, East China, *Environ. Sci. Pollut. Res.*, 2018, **25**(20), 19393–19402, DOI: 10.1007/s11356-018-2124-x.

12 J. H. Zhao, L. X. Hu, Y. Q. Wang, *et al.*, Screening of organic chemicals in surface water of the North River by high resolution mass spectrometry, *Chemosphere*, 2022, **290**, 133174, DOI: 10.1016/j.chemosphere.2021.133174.

13 X. J. Wen, C. G. Niu, L. Zhang, *et al.*, A novel Ag_2O/CeO_2 heterojunction photocatalysts for photocatalytic degradation of enrofloxacin: possible degradation pathways, mineralization activity and an in depth mechanism insight, *Appl. Catal., B*, 2018, **221**, 701–714, DOI: 10.1016/j.apcatb.2017.09.060.

14 A. Fujishima and K. Honda, Electrochemical photolysis of water at a semiconductor electrode, *Nature*, 1972, **238**(5358), 37–38, DOI: 10.1038/238037a0.

15 H. Wang, X. Zhang and Y. Xie, Recent progress in ultrathin two-dimensional semiconductors for photocatalysis, *Mater. Sci. Eng., R*, 2018, **130**, 1–39, DOI: 10.1016/j.mser.2018.04.002.

16 T. P. Yoon, M. A. Ischay and J. Du, Visible light photocatalysis as a greener approach to photochemical synthesis, *Nat. Chem.*, 2010, **2**(7), 527–532, DOI: 10.1038/nchem.687.

17 S. Eustis and M. A. El-Sayed, Why gold nanoparticles are more precious than pretty gold: noble metal surface plasmon resonance and its enhancement of the radiative and nonradiative properties of nanocrystals of different shapes, *Chem. Soc. Rev.*, 2006, **35**(3), 209–217, DOI: 10.1039/b514191e.

18 Z. Xiu, M. Guo, T. Zhao, *et al.*, Recent advances in Ti^{3+} self-doped nanostructured TiO_2 visible light photocatalysts for environmental and energy applications, *Chem. Eng. J.*, 2020, **382**, 123011, DOI: 10.1016/j.cej.2019.123011.

19 S. Y. Mendiola-Alvarez, A. Hernández-Ramírez, J. L. Guzmán-Mar, *et al.*, A novel P-doped Fe_2O_3-TiO_2 mixed oxide: synthesis, characterization and photocatalytic activity under visible radiation, *Catal. Today*, 2019, **328**, 91–98, DOI: 10.1016/j.cattod.2019.01.004.

20 M. N. Chong, B. Jin, C. W. K. Chow, *et al.*, Recent developments in photocatalytic water treatment technology: a review, *Water Res.*, 2010, **44**(10), 2997–3027, DOI: 10.1016/j.watres.2010.02.039.

21 S. Liu, Q. Hu, J. Qiu, *et al.*, Enhanced photocatalytic degradation of environmental pollutants under visible irradiation by a composite coating, *Environ. Sci. Technol.*, 2017, **51**(9), 5137–5145, DOI: 10.1021/acs.est.7b00350.

22 X. Zhao, G. Zhang and Z. Zhang, TiO_2-based catalysts for photocatalytic reduction of aqueous oxyanions: state-of-the-art and future prospects, *Environ. Int.*, 2020, **136**, 105453, DOI: 10.1016/j.envint.2019.105453.

23 W. Wang, J. Fang, S. Shao, *et al.*, Compact and uniform TiO_2@g-C_3N_4 core-shell quantum heterojunction for photocatalytic degradation of tetracycline antibiotics, *Appl. Catal., B*, 2017, **217**, 57–64, DOI: 10.1016/j.apcatb.2017.05.037.

24 J. Liang, X. Yang, Y. Wang, *et al.*, A review on g-C_3N_4 incorporated with organics for enhanced photocatalytic water splitting, *J. Mater. Chem. A*, 2021, **9**(22), 12898–12922, DOI: 10.1039/d1ta00890k.

25 J. Wang and S. Wang, A critical review on graphitic carbon nitride (g-C_3N_4)-based materials: preparation, modification and environmental application, *Coord. Chem. Rev.*, 2022, **453**, 214338, DOI: 10.1016/j.ccr.2021.214338.

26 X. Hu, P. Lu, R. Pan, *et al.*, Metal-ion-assisted construction of cyano group defects in g-C_3N_4 to simultaneously degrade wastewater and produce hydrogen, *Chem. Eng. J.*, 2021, **423**, 130278, DOI: 10.1016/j.cej.2021.130278.

27 T. Liu, L. Hao, L. Bai, *et al.*, Z-scheme junction $Bi_2O_2(NO_3)(OH)$/g-C_3N_4 for promoting CO_2 photoreduction, *Chem. Eng. J.*, 2022, **429**, 132268, DOI: 10.1016/j.cej.2021.132268.

28 M. Wei, L. Yang, Y. Yan, *et al.*, Preparation of ZnS quantum dot photocatalyst and study on photocatalytic degradation of antibiotics, *Mater. Express*, 2019, **9**(5), 413–418, DOI: 10.1166/mex.2019.1518.

29 J. Zhao, M. Ji, H. Chen, *et al.*, Interfacial chemical bond modulated $Bi_{19}S_{27}Br_3$/g-C_3N_4 Z-scheme heterojunction for

enhanced photocatalytic CO_2 conversion, *Appl. Catal., B*, 2022, **307**, 121162, DOI: 10.1016/j.apcatb.2022.121162.

30 Y. Tan, W. Chen, G. Liao, *et al.*, Strategy for Improving Photocatalytic Ozonation Activity of g-C_3N_4 by Halogen Doping for Water Purification, *Appl. Catal., B*, 2022, 121133, DOI: 10.1016/j.apcatb.2022.121133.

31 W. He, L. Liu, T. Ma, *et al.*, Controllable morphology $CoFe_2O_4$/g-C_3N_4 p–n heterojunction photocatalysts with built-in electric field enhance photocatalytic performance, *Appl. Catal., B*, 2022, 121107, DOI: 10.1016/j.apcatb.2022.121107.

32 Y. Xu, F. Ge, Z. Chen, *et al.*, One-step synthesis of Fe-doped surface-alkalinized g-C_3N_4 and their improved visible-light photocatalytic performance, *Appl. Surf. Sci.*, 2019, **469**, 739–746, DOI: 10.1016/j.apsusc.2018.11.062.

33 Q. Su, J. Li, H. Yuan, *et al.*, Visible-light-driven photocatalytic degradation of ofloxacin by g-C_3N_4/NH_2-MIL-88B (Fe) heterostructure: mechanisms, DFT calculation, degradation pathway and toxicity evolution, *Chem. Eng. J.*, 2022, **427**, 131594, DOI: 10.1016/j.cej.2021.131594.

34 L. Atanda, S. Mukundan, A. Shrotri, *et al.*, Catalytic conversion of glucose to 5-hydroxymethyl-furfural with a phosphated TiO_2 catalyst, *ChemCatChem*, 2015, **7**(5), 781–790, DOI: 10.1002/cctc.201402794.

35 W. Yang, L. Jia, P. Wu, *et al.*, Effect of thermal program on structure–activity relationship of g-C_3N_4 prepared by urea pyrolysis and its application for controllable production of g-C_3N_4, *J. Solid State Chem.*, 2021, **304**, 122545, DOI: 10.1016/j.jssc.2021.122545.

36 Y. Wang, W. Yang, X. Chen, *et al.*, Photocatalytic activity enhancement of core-shell structure g-C_3N_4@TiO_2 via controlled ultrathin g-C_3N_4 layer, *Appl. Catal., B*, 2018, **220**, 337–347, DOI: 10.1016/j.apcatb.2017.08.004.

37 X. Zhou, C. Shao, X. Li, *et al.*, Three dimensional hierarchical heterostructures of g-C_3N_4 nanosheets/TiO_2 nanofibers: controllable growth via gas-solid reaction and enhanced photocatalytic activity under visible light, *J. Hazard. Mater.*, 2018, **344**, 113–122, DOI: 10.1016/j.jhazmat.2017.10.006.

38 H. Y. Yuan, Q. Su, Y. H. Wang, *et al.*, Tetracycline catalytic photodegradation with mesoporous phosphated TiO_2: characterization, process optimization and degradation pathway, *RSC Adv.*, 2021, **11**(18), 10975–10985, DOI: 10.1039/d1ra00516b.

39 J. Li, Q. Su, H. Y. Yuan, *et al.*, Photocatalytic degradation of sulfamonomethoxine by mesoporous phosphorus-doped titania under simulated solar light irradiation, *Chemosphere*, 2021, **285**, 131553, DOI: 10.1016/j.chemosphere.2021.131553.

40 S. Moradi, A. A. Isari, F. Hayati, *et al.*, Co-implanting of TiO_2 and liquid-phase-delaminated g-C_3N_4 on multi-functional graphene nanobridges for enhancing photocatalytic degradation of acetaminophen, *Chem. Eng. J.*, 2021, **414**, 128618, DOI: 10.1016/j.cej.2021.128618.

41 C. Xu, D. Li, X. Liu, *et al.*, Direct Z-scheme construction of g-C_3N_4 quantum dots/TiO_2 nanoflakes for efficient photocatalysis, *Chem. Eng. J.*, 2022, **430**, 132861, DOI: 10.1016/j.cej.2021.132861.

42 Q. Wang, L. Zhang, Y. Guo, *et al.*, Multifunctional 2D porous g-C_3N_4 nanosheets hybridized with 3D hierarchical TiO_2 microflowers for selective dye adsorption, antibiotic degradation and CO_2 reduction, *Chem. Eng. J.*, 2020, **396**, 125347, DOI: 10.1016/j.cej.2020.125347.

43 L. Liu, J. Liu, K. Sun, *et al.*, Novel phosphorus-doped Bi_2WO_6 monolayer with oxygen vacancies for superior photocatalytic water detoxication and nitrogen fixation performance, *Chem. Eng. J.*, 2021, **411**, 128629, DOI: 10.1016/j.cej.2021.128629.

44 H. Deng, X. Wang, L. Wang, *et al.*, Enhanced photocatalytic reduction of aqueous Re(VII) in ambient air by amorphous TiO_2/g-C_3N_4 photocatalysts: implications for Tc(VII) elimination, *Chem. Eng. J.*, 2020, **401**, 125977, DOI: 10.1016/j.cej.2020.125977.

45 J. Wang, G. Wang, B. Cheng, *et al.*, Sulfur-doped g-C_3N_4/TiO_2 S-scheme heterojunction photocatalyst for Congo Red photodegradation, *Chin. J. Catal.*, 2021, **42**(1), 56–68, DOI: 10.1016/s1872-2067(20)63634-8.

46 J. Huang, D. Li, R. Li, *et al.*, One-step synthesis of phosphorus/oxygen co-doped g-C_3N_4/anatase TiO_2 Z-scheme photocatalyst for significantly enhanced visible-light photocatalysis degradation of enrofloxacin, *J. Hazard. Mater.*, 2020, **386**, 121634, DOI: 10.1016/j.jhazmat.2019.121634.

47 R. A. Rather, S. Singh and B. Pal, A C_3N_4 surface passivated highly photoactive Au-TiO_2 tubular nanostructure for the efficient H_2 production from water under sunlight irradiation, *Appl. Catal., B*, 2017, **213**, 9–17, DOI: 10.1016/j.apcatb.2017.05.002.

48 W. Zhao, Y. Feng, H. Huang, *et al.*, A novel Z-scheme Ag_3VO_4/$BiVO_4$ heterojunction photocatalyst: study on the excellent photocatalytic performance and photocatalytic mechanism, *Appl. Catal., B*, 2019, **245**, 448–458, DOI: 10.1016/j.apcatb.2019.01.001.

49 K. Zhong, J. Feng, H. Gao, *et al.*, Fabrication of $BiVO_4$@g-C_3N_4(100) heterojunction with enhanced photocatalytic visible-light-driven activity, *J. Solid State Chem.*, 2019, **274**, 142–151, DOI: 10.1016/j.jssc.2019.03.022.

50 W. Wang, J. Fang, S. Shao, *et al.*, Compact and uniform TiO_2@g-C_3N_4 core-shell quantum heterojunction for photocatalytic degradation of tetracycline antibiotics, *Appl. Catal., B*, 2017, **217**, 57–64, DOI: 10.1016/j.apcatb.2017.05.037.

51 Y. Duan, J. Li, Y. Li, *et al.*, Direct Z-scheme $Bi_2O_2CO_3$/porous g-C_3N_4 heterojunction for improved photocatalytic degradation performance, *J. Taiwan Inst. Chem. Eng.*, 2020, **106**, 74–85, DOI: 10.1016/j.jtice.2019.08.013.

52 Y. Yang, Z. Zeng, C. Zhang, *et al.*, Construction of iodine vacancy-rich BiOI/Ag@AgI Z-scheme heterojunction photocatalysts for visible-light-driven tetracycline degradation: transformation pathways and mechanism insight, *Chem. Eng. J.*, 2018, **349**, 808–821, DOI: 10.1016/j.cej.2018.05.093.

53 B. Luo, M. Chen, Z. Zhang, *et al.*, Highly efficient visible-light-driven photocatalytic degradation of tetracycline by a Z-scheme g-C_3N_4/Bi_3TaO_7 nanocomposite photocatalyst,

Dalton Trans., 2017, **46**(26), 8431–8438, DOI: 10.1039/c7dt01250k.

54 Y. Ren, T. Gong, S. Tan, *et al.*, Photocatalytic activities of g-C_3N_4, Bi_3NbO_7 and g-C_3N_4/Bi_3NbO_7 in photocatalytic reduction of Cr(VI), *J. Alloys Compd.*, 2022, 163752, DOI: 10.1016/j.jallcom.2022.163752.

55 W. Ye, J. Hu, X. Hu, *et al.*, Rational Construction of Z-Scheme $CuInS_2$/Au/g-C_3N_4 Heterostructure: Experimental Results and Theoretical Calculation, *ChemCatChem*, 2019, **11**(24), 6372–6383, DOI: 10.1002/cctc.201901227.

56 G. Wang, Y. Li, J. Dai, *et al.*, Highly efficient photocatalytic oxidation of antibiotic ciprofloxacin using TiO_2@g-C_3N_4@biochar composite, *Environ. Sci. Pollut. Res.*, 2022, 1–17, DOI: 10.1007/s11356-022-19269-w.

57 H. Shi, X. Wei, J. Zhang, *et al.*, Green Synthesis and Direct Z-Scheme CdSe/BiOCl Heterojunctions for Enhanced Photocatalytic Performance, *ChemistrySelect*, 2020, **5**(20), 6230–6235, DOI: 10.1002/slct.202001289.

58 C. Ouyang, X. Quan, C. Zhang, *et al.*, Direct Z-scheme $ZnIn_2S_4$@ MoO_3 heterojunction for efficient photodegradation of tetracycline hydrochloride under visible light irradiation, *Chem. Eng. J.*, 2021, **424**, 130510, DOI: 10.1016/j.cej.2021.130510.

59 Z. Pan, L. Qian, J. Shen, *et al.*, Construction and application of Z-scheme heterojunction In_2O_3/Bi_4O_7 with effective removal of antibiotic under visible light, *Chem. Eng. J.*, 2021, **426**, 130385, DOI: 10.1016/j.cej.2021.130385.

60 C. Zhao, Y. Li, H. Chu, *et al.*, Construction of direct Z-scheme Bi_5O_7I/UiO-66-NH_2 heterojunction photocatalysts for enhanced degradation of ciprofloxacin: mechanism insight, pathway analysis and toxicity evaluation, *J. Hazard. Mater.*, 2021, **419**, 126466, DOI: 10.1016/j.jhazmat.2021.126466.

61 H. Mittal and M. Khanuja, Hydrothermal in-situ synthesis of $MoSe_2$-polypyrrole nanocomposite for efficient photocatalytic degradation of dyes under dark and visible light irradiation, *Sep. Purif. Technol.*, 2021, **254**, 117508, DOI: 10.1016/j.seppur.2020.117508.

62 X. Liu, Y. Liu, S. Lu, *et al.*, Performance and mechanism into TiO_2/zeolite composites for sulfadiazine adsorption and photodegradation, *Chem. Eng. J.*, 2018, **350**, 131–147, DOI: 10.1016/j.cej.2018.05.141.

63 S. Sun, H. Yao, W. Fu, *et al.*, Enhanced degradation of antibiotics by photo-fenton reactive membrane filtration, *J. Hazard. Mater.*, 2020, **386**, 121955, DOI: 10.1016/j.jhazmat.2019.121955.

64 Q. Wang, M. Xiao, Z. Peng, *et al.*, Visible LED photocatalysis combined with ultrafiltration driven by metal-free oxygen-doped graphitic carbon nitride for sulfamethazine degradation, *J. Hazard. Mater.*, 2022, 129632, DOI: 10.1016/j.jhazmat.2022.129632.

65 M. Samy, M. G. Ibrahim, M. G. Alalm, *et al.*, Effective photocatalytic degradation of sulfamethazine by CNTs/$LaVO_4$ in suspension and dip coating modes, *Sep. Purif. Technol.*, 2020, **235**, 116138, DOI: 10.1016/j.seppur.2019.116138.

66 Z. Ouyang, C. Yang, J. He, *et al.*, Homogeneous photocatalytic degradation of sulfamethazine induced by Fe(III)-carboxylate complexes: kinetics, mechanism and products, *Chem. Eng. J.*, 2020, **402**, 126122, DOI: 10.1016/j.cej.2020.126122.

67 Y. Song, J. Tian, S. Gao, *et al.*, Photodegradation of sulfonamides by g-C_3N_4 under visible light irradiation: effectiveness, mechanism and pathways, *Appl. Catal., B*, 2017, **210**, 88–96, DOI: 10.1016/j.apcatb.2017.03.059.

68 E. Ioannidou, Z. Frontistis, M. Antonopoulou, *et al.*, Solar photocatalytic degradation of sulfamethoxazole over tungsten-modified TiO_2, *Chem. Eng. J.*, 2017, **318**, 143–152, DOI: 10.1016/j.cej.2016.06.012.

69 S. K. Ray, D. Dhakal and S. W. Lee, Insight into sulfamethoxazole degradation, mechanism, and pathways by AgBr-$BaMoO_4$ composite photocatalyst, *J. Photochem. Photobiol., A*, 2018, **364**, 686–695, DOI: 10.1016/j.jphotochem.2018.07.007.

70 R. Yuan, Y. Zhu, B. Zhou, *et al.*, Photocatalytic oxidation of sulfamethoxazole in the presence of TiO_2: effect of matrix in aqueous solution on decomposition mechanisms, *Chem. Eng. J.*, 2019, **359**, 1527–1536, DOI: 10.1016/j.cej.2018.11.019.

71 J. Guo, L. Wang, X. Wei, *et al.*, Direct Z-scheme $CuInS_2$/Bi_2MoO_6 heterostructure for enhanced photocatalytic degradation of tetracycline under visible light, *J. Hazard. Mater.*, 2021, **415**, 125591, DOI: 10.1016/j.jhazmat.2021.125591.

72 L. Zhang, Y. Meng, T. Dai, *et al.*, Fabrication of a coated $BiVO_4$@LDHs Z-scheme heterojunction and photocatalytic degradation of norfloxacin, *Appl. Clay Sci.*, 2022, **219**, 106435, DOI: 10.1016/j.clay.2022.106435.

73 C. Liu, H. Dai, C. Tan, *et al.*, Photo-fenton degradation of tetracycline over Z-scheme Fe-g-C_3N_4/Bi_2WO_6 heterojunctions: mechanism insight, degradation pathways and DFT calculation, *Appl. Catal., B*, 2022, 121326, DOI: 10.1016/j.apcatb.2022.121326.